Surface & Coatings Technology 513 (2025) 132448

Contents lists available at ScienceDirect

Surface & Coatings Technology

journal homepage: www.elsevier.com/locate/surfcoat

Machine learning enabled the prediction of γ′-depleted depth during interdiffusion of bond-coated IN792 superalloy

Haoyi Xu [a], Xiaoyu Sun [a,*], Ru Lin Peng [b], Johan Moverare [b], Xin-Hai Li [c], Guanshui Ma [a], Zhenyu Wang [a], Aiying Wang [a,*]

[a] State Key Laboratory of Advanced Marine Materials, Zhejiang Key Laboratory of Extreme-environmental Material Surfaces and Interfaces, Ningbo Institute of Materials Technology and Engineering, Chinese Academy of Sciences, Ningbo 315201, China
[b] Department of Management and Engineering, Linköping University, SE-58183 Linköping, Sweden
[c] Siemens Energy AB, SE-61283 Finspång, Sweden

ARTICLE INFO

Keywords:
Machine learning
Thermal barrier coatings (TBCs)
γ′-Depleted zone (GPDZ)
Interdiffusion

ABSTRACT

Eight machine learning (ML) frameworks were established for predicting γ′-depleted zone (GPDZ) evolution in MCrAlY-coated IN792 superalloys, based on the 301 experimental datasets from high-temperature diffusion tests. Thereinto, XGBoost model with Bayesian optimization demonstrated the best performance with a high R^2 of 0.9696 and a low mean absolute error of 3.579. SHAP analysis on the results identified temperature/time as the dominant kinetic drivers, while Ni/Co/Ta suppressed the GPDZ growth and Fe/Cr/Al accelerated the γ′ depletion. The trained model was employed to predict growth kinetics of GPDZ in changes of time and compositions and also was evidenced to direct the coating design with reduced degradation of substrate microstructure. This data-driven approach constructs a strongly efficient tool for the composition-microstructure correlation, overcoming the high-time-cost limitation on the traditional thermodynamic methods in multi-component systems.

1. Introduction

One of great advances in aircraft engine industry is the use of thermal barrier coatings (TBCs) that significantly improves the operating temperature and oxidation resistance of superalloys, the state-of-the-art materials for the core section of turbine blades [1–5]. These advantages are achieved by a ceramic topcoat with a low conductivity and a metallic bond coating [6–10]. MCrAlY (M = Ni and/or Co) coatings, as the typical metallic bond coating materials, contains approximately 50 vol% β-NiAl precipitates as Al reservoirs, facilitating the formation of a dense, continuous and thermal-growth Al_2O_3 layer to inhibit oxidizing-gas penetration [11–13]. Unfortunately, over 1000 °C, a heavy MCrAlY-coating/superalloy (MC/S) interdiffusion often occurs, causing catastrophic degradation of the γ/γ′ microstructure to a γ structure in the substrate and thus the reduction of its mechanical properties [14–16]. For example, coated superalloys exhibit reduced creep or fatigue life compared to uncoated counterparts under identical conditions [17–19]. Hence, the oxidation-resistance advantage from MCrAlY coatings comes at the expense of reduced mechanical properties.

MC/S interdiffusion is a complex element-migration process, involving more than 8 multi-components [20–22], the mutual interference between them [23–25] and the diffusion-induced phase transitions [26–29]. In previous research, thermodynamic simulations were used to predict the γ′-depleted during the coating/superalloy interdiffusion process via calculating phase equilibrium and diffusion step [30–32]. However, the phase-equilibrium calculation is a very time-consuming step, since it requires calculating the minimum Gibbs free energy for each point in the system. Additionally, simulating one case using this method usually takes several weeks or months, up to the complexity of the system. Clearly, it could not meet the rapid demand of numerous calculations for coating design. Given this limitation, machine learning (ML) has emerged as an important complementary approach. ML leverages computer logic to directly construct the mapping relations between the input features (composition, temperature, time) and the output result of γ′-depleted zone [33]. In our work, the most important result was that we established the optimized ML model with high efficiency calculation, enabling the facile predicting γ′-depleted zone (take only several seconds) and providing a broad compositional range for coating design to reduce the detrimental effects from the interdiffusion on superalloys.

* Corresponding authors.
E-mail addresses: sunxiaoyu@nimte.ac.cn (X. Sun), aywang@nimte.ac.cn (A. Wang).

https://doi.org/10.1016/j.surfcoat.2025.132448
Received 7 May 2025; Received in revised form 21 June 2025; Accepted 28 June 2025
Available online 4 July 2025

ML has been expanded into the field of materials science, such as the predictions of microstructure evolution [34,35], corrosion or mechanical properties [35–38], and the optimization of manufacturing parameters [39–42]. Banko et al. [43] employed conditional generative adversarial networks (cGAN) to link sputtering parameters with Cr-Al-O-N film grain sizes, enabling process optimization. Peng et al. [44] proposed a support vector machine (SVM) model to predict oxidation rate constants (k_P) for NiCr-based alloys at a temperature range of 800–950 °C. In coating design, Jia et al. [45] linked 14-dimensional features to wear resistance via XGBoost, highlighting bonding strength ($Lc1$) as a key factor for high-entropy nitrides. Xu et al. [46] applied random forests (RF) to optimize Al/Cr ratios in ultrahard high-entropy ceramics, revealing bias voltage and composition effects on hardness. For performance prediction, Wang et al. [47] combined RF and gradient-boosted trees to decode tribological responses of WS_2 coatings under complex loads, while Ma et al. [48] fused neural networks (ANN) with RF to predict corrosion lifetimes of Cr/GLC coatings (97.9 % accuracy) using electrochemical and porosity data. These studies indicate the unique advantage of ML to investigate complex material system and it is expected the application of ML on the challenge of MC/S interdiffusion.

In this research, we gathered data on the thickness changes of γ′-depletion zone (GPDZ) with temperature, time and composition from a series of high-temperature MC/S interdiffusion experiments. Subsequently, we utilized eight algorithms to establish ML models, i.e., extreme gradient boosting (XGBoost), gradient boosting regression (GBR), random forest (RF), decision tree (DT), multi-layer perceptron (MLP), extreme learning machine (ELM), support vector regression (SVR), and *k*-nearest neighbors (KNN) regression. We further employed Bayesian optimizing method to achieve a precise prediction. Pearson correlation coefficients and SHAP (SHapley Additive exPlanations) values were systematically applied to decode nonlinear contributions of key features. This framework overcomes the dimensionality constraints of traditional single-scale simulations, establishing a cross-scale "composition-process-microstructure" correlation model, thereby providing quantitative guidelines for the design of high-durability coatings.

2. Methods

2.1. Data collection and processing

Fig. 1 illustrates the detailed workflow of this study, encompassing three critical phases: data collection and processing, model training and evaluation, and model analysis and prediction. The dataset of 301 samples used in this research were accessed by a series of high-temperature interdiffusion experiments between MCrAlY coatings and the IN792 superalloy, as show in Table 1. The coatings were deposited on IN792 substrates via high-velocity oxy-fuel (HVOF) spraying. Post-spray heat treatment was performed to optimize the coating-substrate interfacial bonding and microstructure. The chemical compositions of the coatings and IN792 substrate were determined by wavelength-dispersive spectroscopy (WDS). These samples were suffered a long-term, high-temperature oxidation tests in a laboratory furnace at 900, 1000 and 1100 °C for 0–12,000 h. Oxidized specimens were air-cooled, mounted in conductive resin, and polished. GPDZ thickness was measured based on the observed BSE-SEM images (see Supplementary Figs. S1–S3), with 10 measurements per sample averaged to minimize error. The input features include coating compositions, temperatures and diffusion times. The training target is the thickness of GPDZ. Fig. 2 shows the GPDZ distributions in various ranges and more details are provided in Supplementary Fig. S4.

To reduce dimensional disparities among input features, the dataset (excluding GPDZ values) was normalized to a 0–1 range using *Z*-score standardization. This step ensures balanced contributions of all parameters during the training, Normalized data is defined as:

$$z_i = \frac{x_i - \mu}{\sigma} \tag{1}$$

where x_i is the original feature value, μ and σ respectively represents the mean and standard deviation of the features across the dataset, and z_i is the normalized value.

2.2. Model training

ML models were constructed by 8 algorithms (XGBoost, GBR, RF, DT, MLP, ELM, SVR and KNN) from the scikit-learn library in Python. These have covered the current mainstream ML methods, including tree-based ensembles (XGBoost, GBR, RF, DT) for nonlinear feature interactions, neural networks (MLP, ELM) for deep learning, and distance/kernel models (SVR, KNN) for comparability. Four error functions of determination coefficient (R^2), mean absolute error (MAE), mean squared error (MSE) and root mean squared error (RMSE) were used as core metrics to evaluate model's performance. Their expressions are as following:

$$R^2 = 1 - \frac{\sum_{i=1}^{n}(y_i - \hat{y}_i)^2}{\sum_{i=1}^{n}(y_i - \bar{y})^2} \tag{2}$$

$$MAE = \frac{1}{n}\sum_{i=1}^{n}|y_i - \hat{y}_i| \tag{3}$$

$$MSE = \frac{1}{n}\sum_{i=1}^{n}(y_i - \hat{y}_i)^2 \tag{4}$$

$$RMSE = \sqrt{\frac{1}{n}\sum_{i=1}^{n}(y_i - \hat{y}_i)^2} \tag{5}$$

where n is the number of samples, y_i and $\hat{y}_i$ represents the observed and predicted values of the i-th instance, respectively, and $\bar{y}$ denotes the mean of all observed values. R^2 serves as a metric to assess the goodness-of-fit of regression models, with a range from 0 to 1. High R^2 value means a strong correlation between predictions and measurements, while lower RMSE, MSE, and MAE values reflect higher predictive accuracy.

The dataset was randomly partitioned into 70 % training, 15 % validation, and 15 % test sets. The model generalization capability was evaluated by ten-fold cross-validation based on the MAE criterion. Prior to training, preliminary hyperparameter optimization was conducted via manual trial-and-error on account of algorithm-specific characteristics. For tree-based models (XGBoost, GBR, RF, DT), critical parameters governing structural complexity and generalization were adjusted to achieve a better training performance. In DT, the maximum tree depth (*max_depth*) was optimized to balance model complexity and overfitting risk. Random forest (RF) introduced the number of weak learners (*n_estimators*) to mitigate variance through ensemble averaging. Gradient boosting regression (GBR) iteratively refined DT-based weak learners, with *n_estimators* controlling iteration count and *learning_rate* regulating individual tree contributions to balance bias and convergence speed. XGBoost extended GBR by incorporating a leaf-wise regularization term and *min_child_weight* to constrain minimum sample weights in leaf nodes, achieving superior bias-variance trade-offs.

Neural networks (MLP, ELM) were tuned by adjusting hidden layer architectures. MLP utilized two hidden layers with the Rectified Linear Unit (ReLU) activation to construct deep nonlinear mappings, while ELM adopted a single hidden layer with sigmoid activation for computational efficiency. Support vector regression (SVR) employed a radial basis function (RBF) kernel, with regularization parameter C and epsilon-insensitive loss parameter ϵ optimized to balance model complexity and generalization. For *k*-nearest neighbors (KNN), the Minkowski distance metric and *n_neighbors* parameter were adjusted to define local decision boundaries. After optimization on the training and validation sets, final performance was evaluated on the test set.

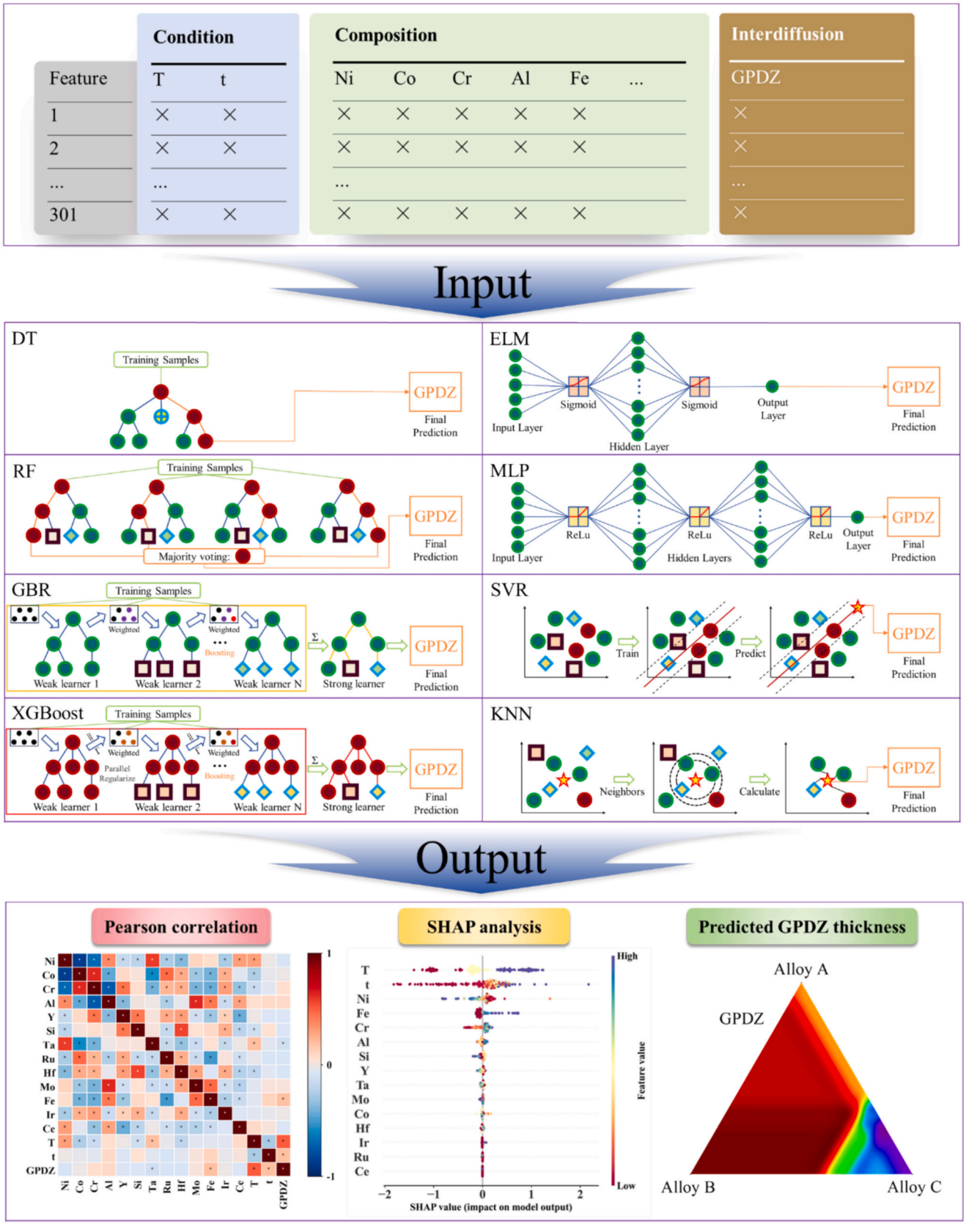

Fig. 1. The workflow of the machine-learning (ML) training. The input features include temperature (T) and time (t) and compositions. The target is the thickness of GPDZ. Subsequently, the model is trained utilizing eight algorithms: XGBoost, GBR, RF, DT, MLP, ELM, SVR and KNN. Finally, the outcomes contain Pearson correlation, SHAP analysis and a "ternary-phase diagram" for GPDZ thickness.

Table 1
The input and target descriptors used in the ML models.

Feature	Range
Coating compositions (wt%)	Ni(31–54.3), Co(12.2–37.8), Cr(13.6–24.2), Al(8–12.8), Y (0–0.8), Si(0–1.4), Ta(0–7.2), Ru(0–0.6), Hf(0–0.4), Mo (0–0.7), Fe(0–9.6), Ir(0–0.6), Ce(0–0.2)
Temperatures (°C)	900–1100
Times (h)	0–12,000
Target (μm)	GPDZ(0–152.02)

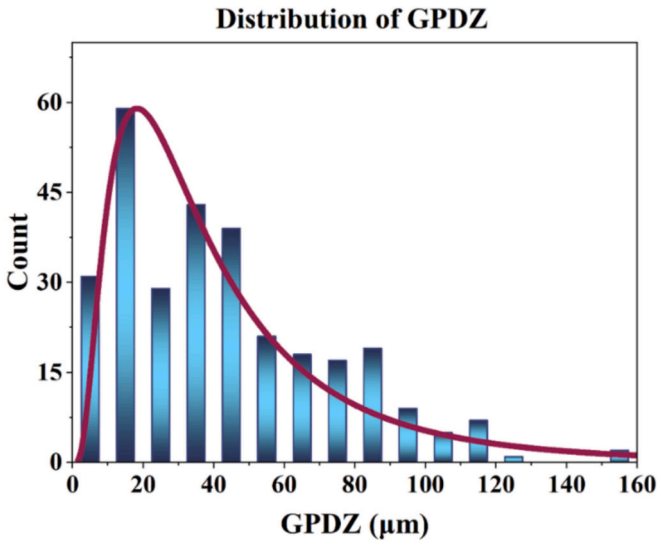

Fig. 2. Distribution of GPDZ values in dataset.

3. Results and discussion

3.1. Comparison of machine learning models

As summarized in Table 2, the performances of eight models were compared based on R^2, MAE, MSE, and RMSE metrics. The XGBoost model achieved the highest predictive accuracy and stability with a lager R^2 of 0.9574 and a small MAE of 4.276. The gradient boosting regression (GBR) model also demonstrated robust performance (R^2 = 0.9534, MAE = 4.4585), validating the effectiveness of gradient boosting in capturing feature interactions. Random forest (RF) and decision tree (DT) yielded R^2 values of 0.9108 and 0.8330, respectively, indicating the adaptability of ensemble methods for nonlinear modeling. DT exhibited significantly higher errors (MAE = 7.7494), suggesting elevated overfitting risks.

In contrast, MLP, ELM, SVR, and KNN displayed weaker generalization. The ELM model exhibited the poorest performance (R^2 = 0.4485, MAE = 15.776), attributable to its fixed hidden-layer architecture and limited parameter flexibility, which hindered its ability to resolve complex nonlinear relationships. MLP partially mitigated this issue via a multi-layer structure (R^2 = 0.5573), though further optimization remains warranted. SVR showed pronounced limitations in nonlinear adaptation (R^2 = 0.5143, MAE = 14.631), reflecting constraints in kernel function selection and hyperplane partitioning. While KNN achieved a marginally higher R^2 (0.5590) than MLP, its reliance on distance metrics rendered it susceptible to high-dimensional noise, resulting in a relatively larger MAE error.

Fig. 3 presents scatter plots comparing predictions and experiments for the eight ML models. Proximity of data points to the central dashed line (y = x) indicates high prediction accuracy. Both XGBoost and GBR exhibit tightly clustered points along the diagonal, particularly in the high-value range (actual >80 μm), demonstrating robust global fitting capabilities. While random forest (RF) maintains concentrated distributions overall, a systematic lower-right deviation is observed in high-value regions, suggesting cumulative underprediction bias for extreme values. The DT model shows concentrated scatter in low-to-medium ranges (actual <50 μm) but significantly increased dispersion in high-value regions, highlighting its inability to resolve extreme-value patterns. Poorer-performing models of MLP, ELM, SVR, and KNN display widespread deviations from the diagonal. Notably, ELM predictions exhibit disordered scattering, corroborating the limitations of shallow network architectures in complex nonlinear tasks.

3.2. Bayesian optimization for XGBoost hyperparameter tuning

Building on the comparative analysis of eight machine learning models in the preceding section, the XGBoost model demonstrated the highest accuracy on the test set (R^2 = 0.9574, MAE = 4.2760). To further enhance its generalization capability, Bayesian optimization was employed for the systematic hyperparameter tuning. Bayesian optimization, a global optimization method based on probabilistic surrogate models, efficiently explores the hyperparameter space within limited iterations by constructing Gaussian process estimations of the objective function. Its core advantage lies in leveraging prior knowledge to guide parameter search directions, significantly reducing computational costs compared to conventional grid search.

The optimization objective was established by utilizing the MAE of the validation set as the fitness function. Key hyperparameters selected for systematic tuning included the number of decision trees (*n_estimators*), maximum tree depth (*max_depth*), and minimum child node weight (*min_child_weight*). The parameter search grid, which outlines the ranges and intervals for these hyperparameters, is comprehensively described in Supplementary Table S2. After 15 iterations of Bayesian optimization, the optimal parameter configuration was determined as *n_estimators* = 173, *max_depth* = 7, and *min_child_weight* = 3.

The Bayesian-optimized XGBoost (XGB-Bay) model exhibited significant performance improvements, as demonstrated in Table 3. The training set R^2 increased to 0.99937, accompanied by a 74.2 % reduction in MAE, indicating markedly enhanced fitting capability to the training data. Concurrently, the cross-validation set MAE decreased by 17.0 %, and the test set MAE decreased by 16.3 %. These enhancements stem from Bayesian optimization's precise control over model complexity: adjusting the number of trees (*n_estimators* = 50 → 173) enhanced ensemble learning robustness, increasing the tree depth (*max_depth* = 5 → 7) strengthened feature interaction capacity, and elevating the minimum child node weight (*min_child_weight* = 1 → 3) effectively mitigated overfitting risks. As illustrated in Fig. 4, the XGB-Bay model achieved near-perfect fitting across the training, cross-validation, and test sets. Training set predictions formed a dense cluster along the diagonal line, while cross-validation and test set predictions exhibited minor dispersion in high-value regions but remained

Table 2
Assessment of ML models.

Model	XGBoost	GBR	RF	DT	KNN	MLP	SVR	ELM
R^2	0.9574	0.9534	0.9108	0.8330	0.5590	0.5573	0.5143	0.4485
MAE	4.276	4.4585	6.0912	7.7494	14.16	13.744	14.631	15.776
MSE	35.321	6.2184	73.944	138.46	365.57	366.96	402.59	457.18
RMSE	5.9432	9.1201	8.599	11.767	19.12	19.156	20.065	21.382

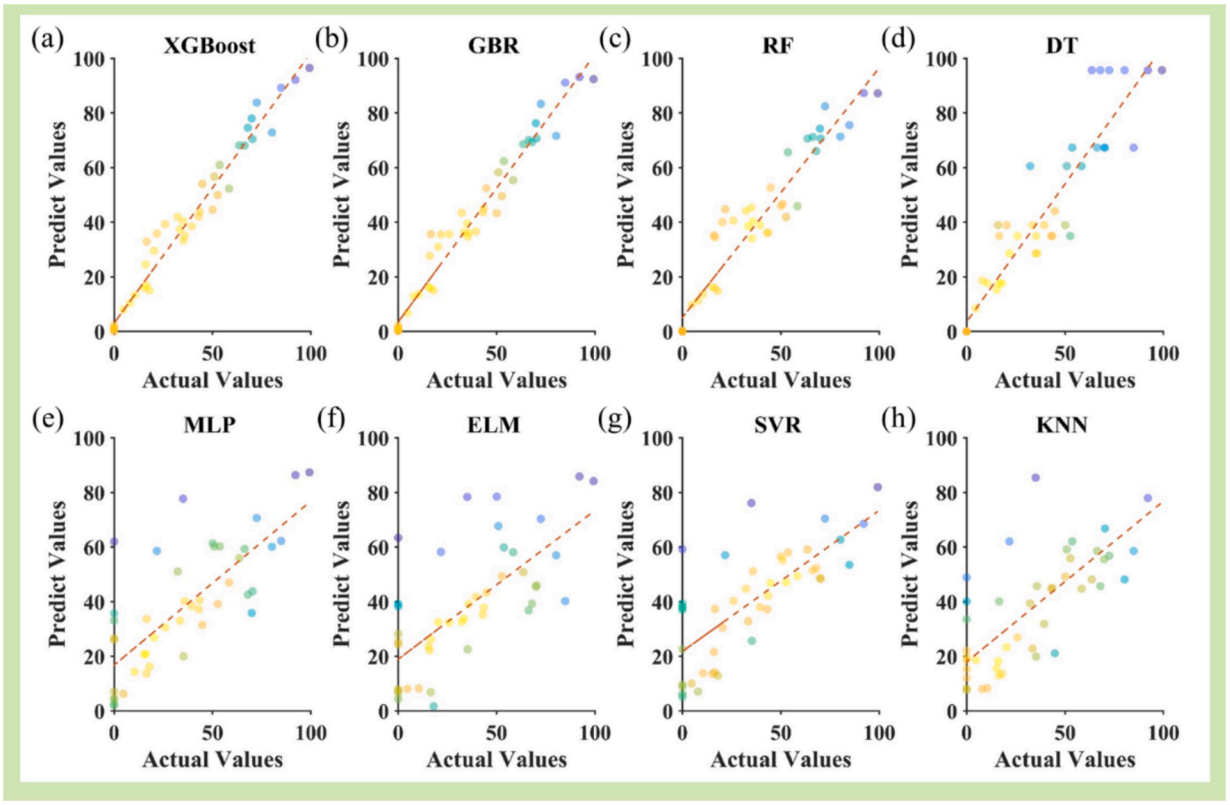

Fig. 3. Comparative analysis of predicted values and actual values on the test set, using (a) XGBoost, (b) GBR, (c) RF, (d) DT, (e) MLP, (f)ELM, (g) SVR and (h) KNN models.

Table 3
Performance comparison between XGBoost and XGB-Bay models.

Model	R^2(train)	MAE (train)	R^2(*k*-fold)	MAE(*k*-fold)	R^2(test)	MAE (test)
XGBoost	0.99031	2.0633	0.97237	3.7516	0.95739	4.2760
XGB-Bay	0.99937	0.53215	0.97711	3.1126	0.96959	3.5788

tightly distributed around the regression line. These observations confirm that the optimized model retains robust nonlinear modeling capabilities while suppressing overfitting. The lower panel of Fig. 4 compares data distributions across subsets. The training set (211 samples), cross-validation set (45 samples), and test set (45 samples) exhibited highly consistent numerical ranges with the original dataset, as evidenced by negligible deviations in kurtosis and skewness. This validates the rationality of data partitioning and the reliability of model generalization.

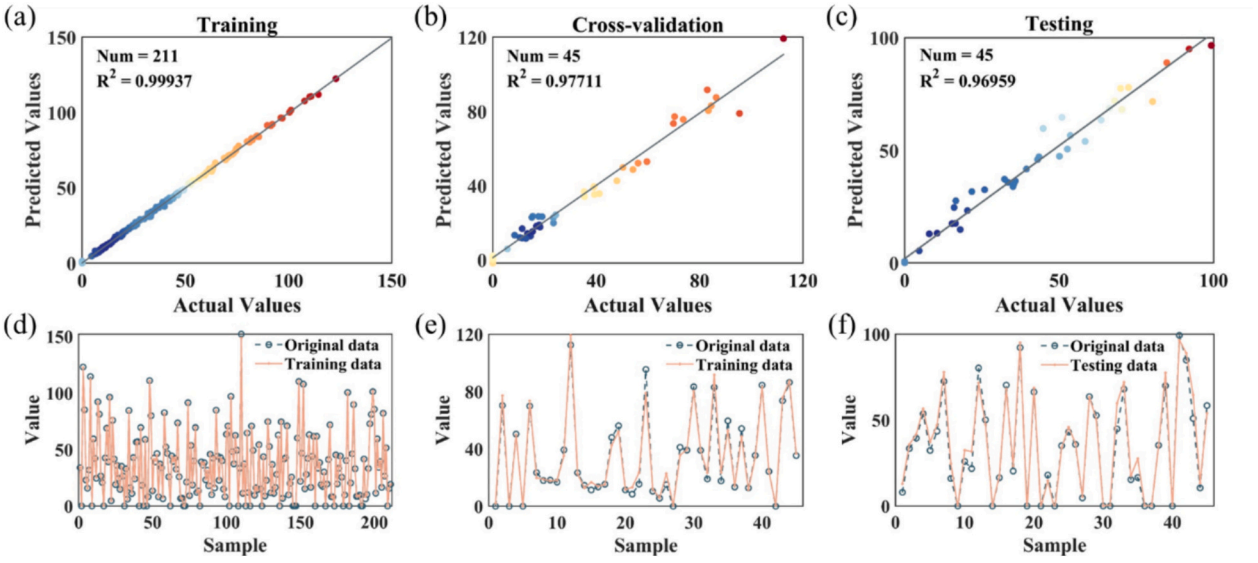

Fig. 4. Performance evaluation on the Bayesian-optimized XGBoost model in training, cross-validation, and testing sets, respectively.

3.3. Analysis of feature importance

To elucidate the influences of input features on the GPDZ target, Pearson correlation coefficient (PCC) analysis was employed to evaluate linear correlations between them, as illustrated in Fig. 5a and detailed in Supplementary Table S3. PCC values range from −1 to 1, with absolute values closer to 1 indicating stronger correlations. Feature pairs exhibiting high PCCs were screened and compiled in Supplementary Table S4, where a threshold of $|PCC| \geq 0.7$ was adopted to define strong inter-feature correlations and asterisks (*) denote p-values <0.05, confirming that the correlations between variables are statistically significant. A strong negative correlation was observed between Ni and Co, as well as between Cr and Al. Because Co was the neighboring element of Ni in the periodic table of elements and they played a similar role as matrix element in the Ni-based superalloys [49,50]. The negative correlation between Cr and Al was attributed to the Al—Cr interference effect on their chemical potentials during the interdiffusion [25,31].

Fig. 5b ranks the top ten features by absolute PCC values, revealing that temperature is the most relevant parameter ($|PCC| = 0.51$), followed by time, Fe content, and Ta content. Fig. 5c illustrates the data distribution of Fe and Ta, which exhibit the highest absolute PCCs among all coating elements. The addition of Fe significantly increases the GPDZ thickness , because Fe promote the phase transition $\gamma' \rightarrow \gamma$ or β. In comparison, Ta shows a reverse effect, since Ta acts a role of the γ' stabilized element that impedes the γ' degradation.

Although Pearson correlation coefficients reveal linear associations

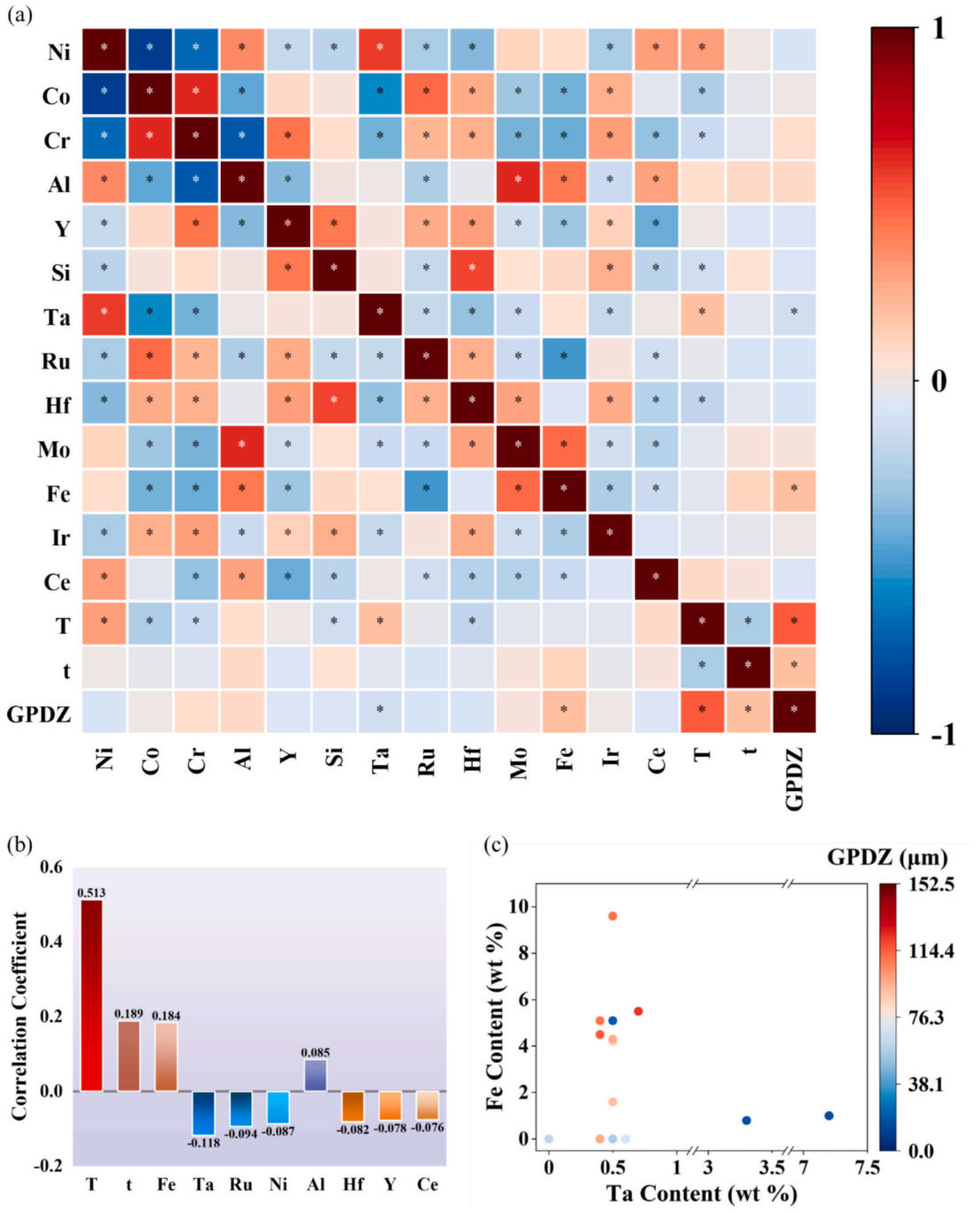

Fig. 5. Feature correlation and input data distribution analysis. (a) Correlation matrix of all features; (b) Top 10 features ranked by correlation coefficient magnitude; (c) Input data distribution stratified by Fe and Ta contents.

between features and the target variable (GPDZ thickness), they cannot adequately quantify the interaction effects and directional contributions of features in multivariate nonlinear systems. The significance analysis in Fig. 5a indicates that only temperature, time, Fe and Ta possess the *p*-values less than 0.05, which means the other features are not statistically significant in terms of their correlation with GPDZ. To address this limitation, SHAP (SHapley Additive exPlanations) analysis was performed on the XGB-Bay model to quantify the global contribution of the input features on the GPDZ target by calculating robust feature importance interpretation in nonlinear contexts. As shown in Fig. 6a, features with higher absolute SHAP values mean stronger influences on GPDZ thickness. The top five influential features are temperature (*T*), time (*t*), Ni content, Fe content, and Cr content, with Ni content being the most critical among coating elements.

To further elucidate mechanistic insights, SHAP visualization was employed to illustrate feature-specific positive/negative correlations. The SHAP summary plot (Fig. 6b) represents each sample as a point, where the x-axis denotes standardized SHAP values (−2.0 to 2.0) reflecting the relative impact of features on model predictions: negative values indicate inhibitory effects on GPDZ thickness, while positive values denote promotive effects. The y-axis ranks the 15 input features, with color gradients (blue to red) representing feature values from high to low. As illustrated in Fig. 6b, SHAP values increase with rising *T* and *t* demonstrating a positive correlation with GPDZ thickness. Temperature accelerates GPDZ growth by enhancing the elemental diffusion rates [6]. And time governs GPDZ expansion through kinetically controlled diffusion distances ($\Delta_{\gamma'} \propto \sqrt{Dt}$) [31]. Fe, Cr and Al concentrations exhibit positive correlations with GPDZ thickness. In contrast, elevated Ni, Co, Si, Y, Ta, and Mo concentrations correlate negatively with GPDZ values. These observations are consistent with established findings regarding the critical roles of Fe, Cr, Ni, and Co in γ'-phase stability and interdiffusion kinetics reported in previous studies [3,23,25,51]. Notably, the weaker Ta and Al effects identified in our ML model compared to their traditionally recognized strong impacts on GPDZ evolution [30,31,49,50,52] could be attributed to dataset limitations-specifically, insufficient high-Ta specimens (present >1 % in only 3 % of samples) and constrained Al variation range (8–12.8 wt%). This data sparsity likely hindered the model's ability to fully capture their characteristic phase-stabilization mechanisms. Interestingly, our model revealed previously underreported inhibitory effects of elevated Si, Y, and Mo concentrations on GPDZ growth, a novel finding warranting experimental validation through controlled diffusion couples in future research. Hf, Ir, Ru, and Ce exhibited negligible correlations consistent with their low concentrations (<0.6 wt%) and limited diffusivity in the Ni-rich matrix.

3.4. Applications

3.4.1. Evidence of kinetics prediction

The growth kinetics of GPDZ during the interdiffusion in the B1, B2, and B4 coated IN792 superalloys at 1000 °C were predicted based on the XGB-Bay model (Fig. 7). The results exhibited a stair-shape increasing trend (blue solid curves in Fig. 7), which is against the continuous growth law of GPDZ. This deviation arises from two factors: data sparsity within specific time-temperature domains and the inherent characteristics of tree-based models. As XGB-Bay employs decision trees as base learners, abrupt changes in output may occur when input parameters cross threshold values defined by the tree-splitting criteria.

To reconcile the ML predictions with fundamental diffusion dynamics, the model outputs were further refined using a power-law fitting function (red dashed curves in Fig. 7) [53,54]. Supplementary Table S5 compares the predicted and refined GPDZ values at five time points (0, 100, 500, 1000, 1500 h). While the refined results exhibited marginally higher mean squared errors (MAE: 0.474–1.255) compared to direct ML predictions (MAE: 0.174–0.686) at these discrete points (Table 4), the fitted curves effectively captured the progressive deceleration in GPDZ growth kinetics, consistent with the power-law dependence of interdiffusion-driven phase evolution. These results demonstrate that while raw ML predictions may exhibit localized discontinuities stair-shape results due to algorithmic constraints, post-processing through physics-informed fitting functions can effectively reconcile data-driven predictions with continuum diffusion principles. The combined ML-fitting framework retains the advantages of high computational efficiency while ensuring physically plausible kinetic predictions.

3.4.2. Concept of coating design

The XGB-Bay predicted results with the key impacting compositions of Ni, Fe, and Cr at 1100 °C for 500 h, are illustrated in a "ternary-phase diagram" (Fig. 8a), where the vertex corresponds to the maximum concentration of the specie (Ni, Fe, or Cr), and color gradients represents the changes of the predicted GPDZ thickness. The increases of both Fe and Cr can promote the γ' depletion, while Ni shows an inverse influence. Complementing these findings, Supplementary Fig. S6 extends the analysis to 900 °C and 1100 °C, further revealing the temperature-dependent interplay between alloy composition and GPDZ evolution.

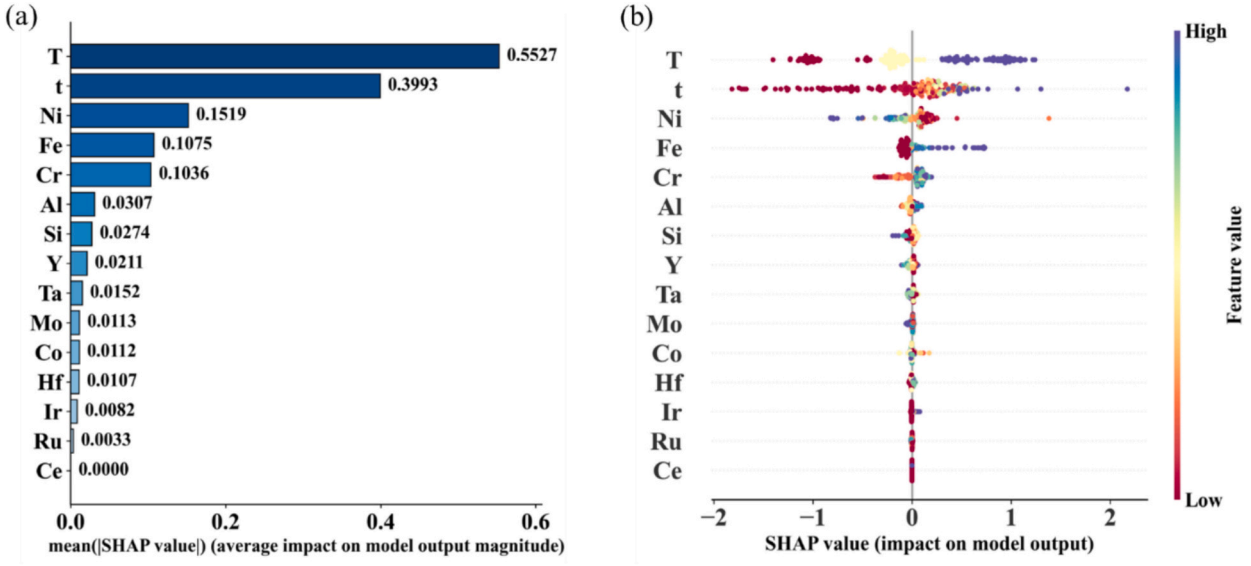

Fig. 6. SHAP analysis results, including (a) feature importance ranking and (b) Summary plot of feature impacts.

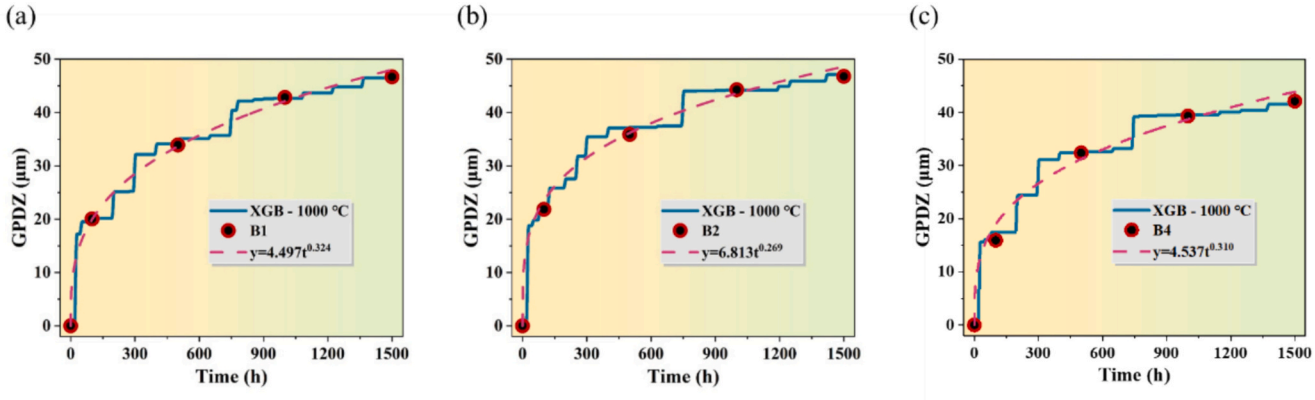

Fig. 7. The predicted GPDZ evolution with time in the (a) B1-, (b) B2-, and (c) B4-coated IN792 superalloy at 1000 °C. The plotted red points denote experimental data from the dataset.

Table 4
MAE evaluation of ML predictions and refined results.

Sample	Predicted MAE (μm)	Refined MAE (μm)
B1	0.186	0.474
B2	0.520	0.888
B4	0.580	1.312

At 900 °C, the ternary diagram shows Cr exerts a weak positive correlation with GPDZ thickening. However, as temperature escalates to 1100 °C, Cr's role intensifies: its contribution to γ′ depletion becomes comparable to Fe. This thermal activation effect aligns with the enhanced interdiffusion kinetics at higher temperatures.

It should be noted that the predicted results in the monochromatic regions are unreliable, due to the limited composition ranges in the current dataset. An effective predicted region (as marked in Fig. 8a) was sectioned from the whole diagram through database analysis. The obtained data from 1000 °C/500 h interdiffusion tests were employed to validate these predicted results in the sectioned region. A high alignment between the predicted and measured values can be observed in Fig. 8b, confirming the model's robustness in capturing primary Ni-Fe-Cr competitive interactions governing GPDZ evolution. Minor deviations in coatings are attributed to secondary influences from other elements: B0, B1, B2, B3, and B4 coatings exhibited elevated GPDZ values due to the absence of Ta (a γ′-stabilizing element), while D72 coating showed increased GPDZ thickness resulting from its low Co content and relatively higher Al concentration compared to B13.

The results above demonstrate the reliability of XGB-Bay ML predicted GPDZ distributions across MCrAlY coating systems. Modern aeroengines demand thermal barrier coatings (TBCs) that synergistically combine oxidation resistance and substrate stability under extreme conditions. Fig. 9a illustrates the GPDZ thickness-composition relationship for B13 coatings at 1000 °C/168 h, with over 80 % of the validated prediction zone exhibiting a low GPDZ thickness <20 μm. Comparative analysis with the high-temperature-oxidation ML model in Ref. [55] (Fig. 9b), which maps $\ln k_p$ values to evaluate oxidation resistance in Ni-Fe-Cr systems, reveals an overlapping blue region (GPDZ <20 μm and $\ln k_p < -14.1$) in both studies. This convergence identifies a composition window (Ni:68–78 wt%, Cr:22–32 wt%, Fe:0–10 wt%) that simultaneously achieves a superior oxidation resistance and also a great

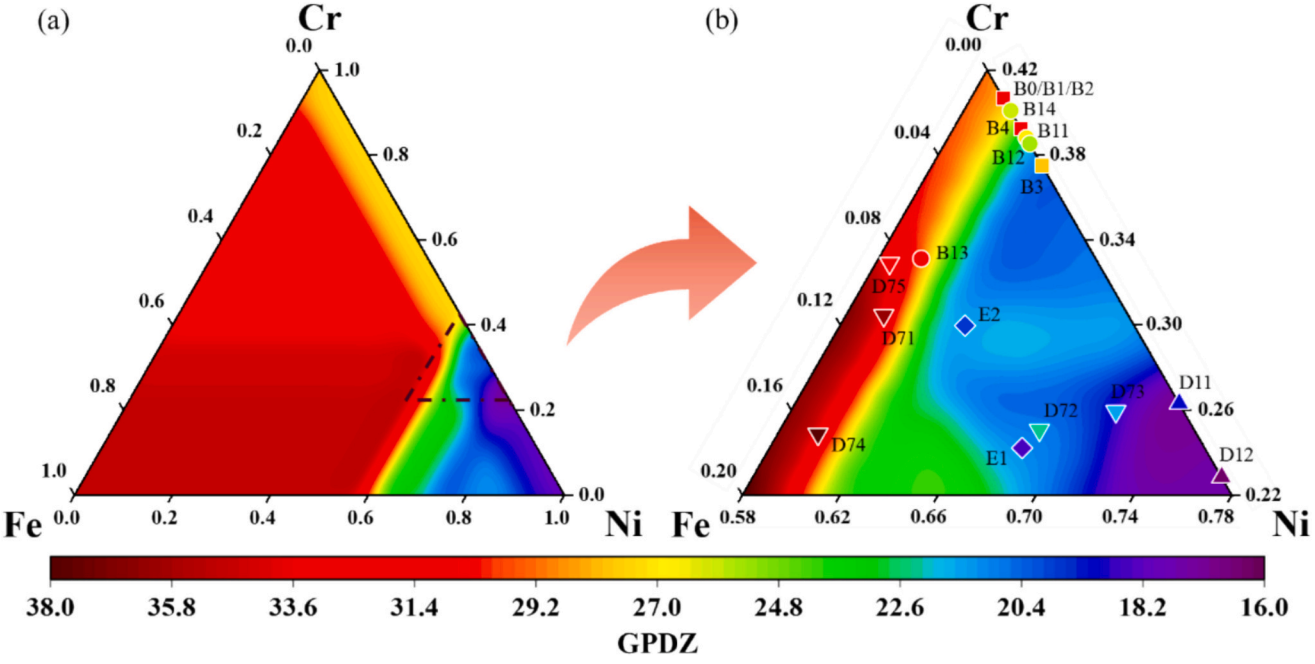

Fig. 8. GPDZ thickness predictions under compositional variations of Ni, Cr, and Fe in B13-coated samples at 1000 °C for 500 h. Contour plots illustrate the systematic modulation of GPDZ thickness in response to Ni, Cr, and Fe content adjustments.

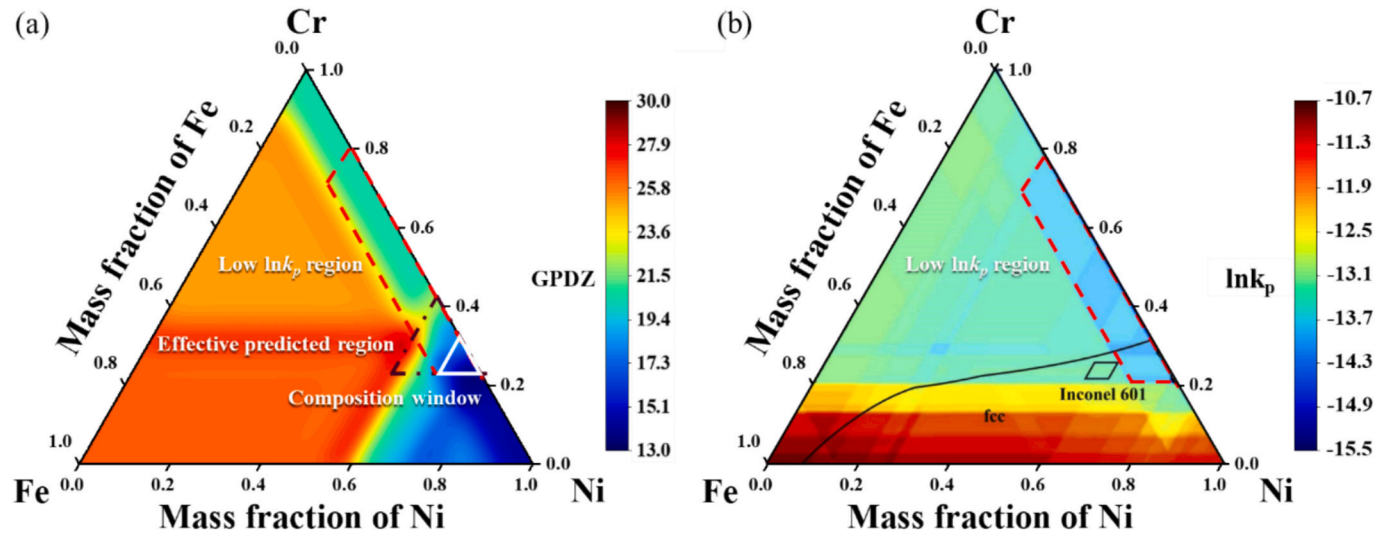

Fig. 9. (a) XGB-Bayesian model predictions of GPDZ thicknesses in B13 coatings at 1000 °C for 168 h, plotted as a function of Ni-Fe-Cr compositional space. (b) Gradient-boosting (GB) model-derived lnk_p predictions for the Ni-Fe-Cr system in Inconel 601 substrate under identical thermal exposure (1000 °C, 168 h) [55]. The black parallelogram represents the Fe-Cr-Ni compositional region of Inconel 601, while the area within the black solid line indicates the *fcc* phase region.

microstructural stability, demonstrating our model's utility in guiding TBCs design.

Compared with traditional thermodynamic approaches, Our ML model provides a high-efficiency alternative enabling rapid GPDZ prediction with 99 % less computational time than CALPHAD-based simulations. It resolves multicomponent competitive interactions while retaining interpretability through SHAP analysis. Current limitations arise from dataset sparsity in high-temperature regimes and unmodeled microstructural factors. Future efforts will integrate active learning with high-throughput experiments to expand predictive accuracy across broader composition-temperature space.

4. Conclusions

In this research, eight ML frameworks were pioneered to predict γ′-depleted zone (GPDZ) evolution during the interdiffusion in the MCrAlY-coated IN792 superalloys, where the 301 experimental datasets were especially established from high-temperature tests. By combining the ML and experimental results, the following conclusions could be clarified:

(1) The XGBoost model optimized via Bayesian optimization demonstrated the superior predictive accuracy ($R^2 = 0.9696$, MAE = 3.579) on the dependence of GPDZ on time, temperature and chemical compositions.
(2) Pearson correlation and SHAP analysis revealed the dominant kinetic drivers of temperature and time, the suppressed roles of Ni, Co, and Ta, as well as the accelerated influences of Fe, Cr, and Al on the growth of GPDZ, which were consistent with the prior reports of Al-Cr chemical potential coupling and Fe-induced γ′→γ phase transitions.
(3) The refined model was not only employed to predict the growth kinetics of GPDZ with temperature, time and compositions, but also strongly evidenced to direct the coating design with the lower interdiffusion-induced microstructural degradation.
(4) Although the ML model identified the robust predictive performance within the tested parameter range, its accuracy still remains contingent on the quality of the dataset. Future work will focus on employing high-throughput experiments to establish comprehensive and precise databases, thereby improving the model accuracy and generalizability to support the optimization strategy of next-generation bond coatings.

CRediT authorship contribution statement

Haoyi Xu: Writing – review & editing, Writing – original draft, Methodology, Investigation, Data curation, Conceptualization. **Xiaoyu Sun:** Writing – review & editing, Validation, Supervision, Resources, Methodology, Funding acquisition, Conceptualization. **Ru Lin Peng:** Resources, Data curation. **Johan Moverare:** Resources, Data curation. **Xin-Hai Li:** Resources, Data curation. **Guanshui Ma:** Writing – review & editing, Validation, Supervision. **Zhenyu Wang:** Writing – review & editing, Validation, Supervision. **Aiying Wang:** Writing – review & editing, Supervision, Resources, Methodology, Funding acquisition.

Declaration of competing interest

The authors declare that they have no known competing financial interests or personal relationships that could have appeared to influence the work reported in this paper.

Acknowledgements

This work was supported by the financial support of the National Science Fund for Distinguished Young Scholars of China (No. 52025014) and the National Key Research and Development Program of China (No. 2024YFB3816500). X. Sun would like to acknowledge the financial support from Siemens Industrial Turbomachinery AB (Finspång, Sweden) and Stiftelsen Axel Hultgrens Fond (Stockholm, Sweden).

Appendix A. Supplementary data

Supplementary data to this article can be found online at https://doi.org/10.1016/j.surfcoat.2025.132448.

Data availability

The raw/processed data required to reproduce these findings cannot be shared at this time as the data also forms part of an ongoing study.

References

[1] N.P. Padture, M. Gell, E.H. Jordan, Thermal barrier coatings for gas-turbine engine applications, Science 296 (2002) 280–284, https://doi.org/10.1126/science.1068609.

[2] Y. Chen, X. Zhao, P. Xiao, Effect of microstructure on early oxidation of MCrAlY coatings, Acta Mater. 159 (2018) 150–162, https://doi.org/10.1016/j.actamat.2018.08.018.

[3] C.E. Campbell, W.J. Boettinger, U.R. Kattner, Development of a diffusion mobility database for Ni-base superalloys, Acta Mater. 50 (2002) 775–792, https://doi.org/10.1016/S1359-6454(01)00383-4.

[4] R.C. Reed, The Superalloys: Fundamentals and Applications, Cambridge University Press, 2006.

[5] K.M. Doleker, Y. Ozgurluk, Y. Kahraman, A.C. Karaoglanli, Oxidation and hot corrosion resistance of HVOF/EB-PVD thermal barrier coating system, Surf. Coat. Technol. 409 (2021) 126862, https://doi.org/10.1016/j.surfcoat.2021.126862.

[6] L.Y. Lim, S.A. Meguid, Temperature dependent dynamic growth of thermally grown oxide in thermal barrier coatings, Mater. Des. 164 (2019) 107543, https://doi.org/10.1016/j.matdes.2018.107543.

[7] G. Bolelli, M.G. Righi, M.Z. Mughal, R. Moscatelli, O. Ligabue, N. Antolotti, M. Sebastiani, L. Lusvarghi, E. Bemporad, Damage progression in thermal barrier coating systems during thermal cycling: a nano-mechanical assessment, Mater. Des. 166 (2019) 107615, https://doi.org/10.1016/j.matdes.2019.107615.

[8] A. Pakseresht, F. Sharifianjazi, A. Esmaeilkhanian, L. Bazli, M. Reisi Nafchi, M. Bazli, K. Kirubaharan, Failure mechanisms and structure tailoring of YSZ and new candidates for thermal barrier coatings: a systematic review, Mater. Des. 222 (2022) 111044, https://doi.org/10.1016/j.matdes.2022.111044.

[9] O. Odabas, A.C. Karaoglanli, Y. Ozgurluk, G. Binal, D. Ozkan, Evaluation of AlCoCrFeNiTi-high entropy alloy (HEA) as top coat material in thermal barrier coating (TBC) system and investigation of its high temperature oxidation behavior, Surf. Coat. Technol. 495 (2025) 131569, https://doi.org/10.1016/j.surfcoat.2024.131569.

[10] Y. Ozgurluk, A. Gulec, D. Ozkan, G. Binal, A. Cahit Karaoglanli, Structural characteristics, oxidation performance and failure mechanism of thermal barrier coatings fabricated by atmospheric plasma spraying and detonation gun spraying, Eng. Fail. Anal. 152 (2023) 107499, https://doi.org/10.1016/j.engfailanal.2023.107499.

[11] P. Richer, M. Yandouzi, L. Beauvais, B. Jodoin, Oxidation behaviour of CoNiCrAlY bond coats produced by plasma, HVOF and cold gas dynamic spraying, Surf. Coat. Technol. 204 (2010) 3962–3974, https://doi.org/10.1016/j.surfcoat.2010.03.043.

[12] D. Toma, W. Brandl, U. Köster, Studies on the transient stage of oxidation of VPS and HVOF sprayed MCrAlY coatings, Surf. Coat. Technol. 120-121 (1999) 8–15, https://doi.org/10.1016/S0257-8972(99)00332-1.

[13] A.C. Karaoglanli, Y. Ozgurluk, K.M. Doleker, Comparison of microstructure and oxidation behavior of CoNiCrAlY coatings produced by APS, SSAPS, D-gun, HVOF and CGDS techniques, Vacuum 180 (2020) 109609, https://doi.org/10.1016/j.vacuum.2020.109609.

[14] M.C. Galetz, C. Oskay, S. Madloch, Microstructural degradation and interdiffusion behavior of NiAl and Ge-modified NiAl coatings deposited on alloy 602 CA, Surf. Coat. Technol. 364 (2019) 211–217, https://doi.org/10.1016/j.surfcoat.2019.02.048.

[15] Y. Liu, M. Zou, H. Su, L. Geng, Y. Yu, W. Zheng, Y. Pei, S. Li, S. Gong, H. Zhang, Coating-associated microstructure evolution and elemental interdiffusion behavior at a Mo-rich nickel-based superalloy, Surf. Coat. Technol. 411 (2021) 127005, https://doi.org/10.1016/j.surfcoat.2021.127005.

[16] J.E. Morral, M.S. Thompson, Interdiffusion and coating design, Surf. Coat. Technol. 43-44 (1990) 371–380, https://doi.org/10.1016/0257-8972(90)90089-U.

[17] L. Han, S. Zheng, M. Tao, C. Fei, Y. Hu, B. Huang, L. Yuan, Service damage mechanism and interface cracking behavior of Ni-based superalloy turbine blades with aluminized coating, Int. J. Fatigue 153 (2021) 106500, https://doi.org/10.1016/j.ijfatigue.2021.106500.

[18] D. Shi, J. Song, H. Qi, S. Li, X. Yang, Effect of interface diffusion on low-cycle fatigue behaviors of MCrAlY coated single crystal superalloys, Int. J. Fatigue 137 (2020) 105660, https://doi.org/10.1016/j.ijfatigue.2020.105660.

[19] Y. Liu, Y. Ru, H. Zhang, Y. Pei, S. Li, S. Gong, Coating-assisted deterioration mechanism of creep resistance at a nickel-based single-crystal superalloy, Surf. Coat. Technol. 406 (2021) 126668, https://doi.org/10.1016/j.surfcoat.2020.126668.

[20] Y. Zhang, J.P. Stacy, B.A. Pint, J.A. Haynes, B.T. Hazel, B.A. Nagaraj, Interdiffusion behavior of Pt-diffused $\gamma+\gamma'$ coatings on Ni-based superalloys, Surf. Coat. Technol. 203 (2008) 417–421, https://doi.org/10.1016/j.surfcoat.2008.08.053.

[21] P. Kiruthika, S.K. Makineni, C. Srivastava, K. Chattopadhyay, A. Paul, Growth mechanism of the interdiffusion zone between platinum modified bond coats and single crystal superalloys, Acta Mater. 105 (2016) 438–448, https://doi.org/10.1016/j.actamat.2015.12.014.

[22] P. Zhang, R. Lin Peng, X.-H. Li, S. Johansson, Investigation of element effect on high-temperature oxidation of HVOF NiCoCrAlX coatings, Coatings 8 (2018) 129, https://doi.org/10.3390/coatings8040129.

[23] K. Yuan, R. Lin Peng, X.-H. Li, S. Johansson, Y.-D. Wang, Some aspects of elemental behaviour in HVOF MCrAlY coatings in high-temperature oxidation, Surf. Coat. Technol. 261 (2015) 86–101, https://doi.org/10.1016/j.surfcoat.2014.11.053.

[24] C.E. Campbell, J.-C. Zhao, M.F. Henry, Comparison of experimental and simulated multicomponent Ni-base superalloy diffusion couples, J. Phase Equilibria Diffus. 25 (2004) 6–15, https://doi.org/10.1007/s11669-004-0167-9.

[25] P. Zhang, X.-H. Li, J. Moverare, R.L. Peng, The iron effect on oxidation and interdiffusion behaviour in MCrAlX coated Ni-base superalloys, Mater. Des. 166 (2019) 107599, https://doi.org/10.1016/j.matdes.2019.107599.

[26] N. Esakkiraja, A. Gupta, V. Jayaram, T. Hickel, S.V. Divinski, A. Paul, Diffusion, defects and understanding the growth of a multicomponent interdiffusion zone between Pt-modified B2 NiAl bond coat and single crystal superalloy, Acta Mater. 195 (2020) 35–49, https://doi.org/10.1016/j.actamat.2020.04.016.

[27] R.R. Adharapurapu, J. Zhu, V.S. Dheeradhada, D.M. Lipkin, T.M. Pollock, Effective Hf-Pd co-doped β-NiAl(Cr) coatings for single-crystal superalloys, Acta Mater. 76 (2014) 449–462, https://doi.org/10.1016/j.actamat.2014.03.001.

[28] N. Czech, F. Schmitz, W. Stamm, Improvement of MCrAlY coatings by addition of rhenium, Surf. Coat. Technol. 68-69 (1994) 17–21, https://doi.org/10.1016/0257-8972(94)90131-7.

[29] P. Audigié, A. Rouaix-Vande Put, H. Murakami, D. Monceau, Chromium and iridium effects on the short-term interdiffusion behaviour between Pt rich γ-γ' bond-coatings and a Ni-Al-Cr alloy, Surf. Coat. Technol. 309 (2017) 258–265, https://doi.org/10.1016/j.surfcoat.2016.11.028.

[30] X. Sun, P. Zhang, J. Moverare, X.-H. Li, L. Cui, R. Lin Peng, Impeding the γ' depletion during the interdiffusion between bond coatings and superalloys via introduction of tantalum in bond coatings, Mater. Des. 227 (2023) 111792, https://doi.org/10.1016/j.matdes.2023.111792.

[31] X. Sun, X. Li, S. Guo, X. Yu, L. Zhu, J. Teng, L. Jiang, J. Moverare, X.-H. Li, R. L. Peng, Revealing microstructural degradation mechanism induced by interdiffusion between Amdry365 coating and IN792 superalloy, Mater. Des. 241 (2024) 112937, https://doi.org/10.1016/j.matdes.2024.112937.

[32] A. Borgenstam, L. Höglund, J. Ågren, A. Engström, DICTRA, a tool for simulation of diffusional transformations in alloys, J. Phase Equilibria 21 (2000) 269–280, https://doi.org/10.1361/105497100770340057.

[33] Z. Wang, Z. Sun, H. Yin, X. Liu, J. Wang, H. Zhao, C.H. Pang, T. Wu, S. Li, Z. Yin, X. Yu, Data-driven materials innovation and applications, Adv. Mater. 34 (2022) 2104113, https://doi.org/10.1002/adma.202104113.

[34] M. Pinz, G. Weber, J.C. Stinville, T. Pollock, S. Ghosh, Data-driven bayesian model-based prediction of fatigue crack nucleation in Ni-based superalloys, Npj Comput. Mater. 8 (2022) 39, https://doi.org/10.1038/s41524-022-00727-5.

[35] Z. Cao, Q. Liu, Q. Liu, X. Yu, J.J. Kruzic, X. Li, A machine learning method to quantitatively predict alpha phase morphology in additively manufactured Ti-6Al-4V, npj Comput. Mater. 9 (2023) 195, https://doi.org/10.1038/s41524-023-01152-y.

[36] M.M.H. Imran, S. Jamaludin, A.F. Mohamad Ayob, A critical review of machine learning algorithms in maritime, offshore, and oil & gas corrosion research: a comprehensive analysis of ANN and RF models, Ocean Eng. 295 (2024) 116796, https://doi.org/10.1016/j.oceaneng.2024.116796.

[37] P.V. Madhavan, S. Shahgaldi, X. Li, Modelling anti-corrosion coating performance of metallic bipolar plates for PEM fuel cells: a machine learning approach, Energy AI 17 (2024) 100391, https://doi.org/10.1016/j.egyai.2024.100391.

[38] V.I. Kolesnikov, D.M. Pashkov, O.A. Belyak, A.A. Guda, S.A. Danilchenko, D. S. Manturov, E.S. Novikov, O.V. Kudryakov, S.A. Guda, A.V. Soldatov, I. V. Kolesnikov, Design of double layer protective coatings: finite element modeling and machine learning approximations, Acta Astronaut. 204 (2023) 869–877, https://doi.org/10.1016/j.actaastro.2022.11.007.

[39] B. Dikici, R. Tuntas, An artificial neural network (ANN) solution to the prediction of age-hardening and corrosion behavior of an Al/TiC functional gradient material (FGM), J. Compos. Mater. 55 (2021) 303–317, https://doi.org/10.1177/0021998320948945.

[40] V. Delchevalerie, N. De Moor, L. Rassinfosse, E. Haye, B. Frenay, S. Lucas, When magnetron sputtering deposition meets machine learning: application to process anomaly detection, Surf. Coat. Technol. 477 (2024) 130301, https://doi.org/10.1016/j.surfcoat.2023.130301.

[41] J.-S. Lim, W.-J. Oh, C.-M. Lee, D.-H. Kim, Selection of effective manufacturing conditions for directed energy deposition process using machine learning methods, Sci. Rep. 11 (2021) 24169, https://doi.org/10.1038/s41598-021-03622-z.

[42] G. Kimaev, L.A. Ricardez-Sandoval, Nonlinear model predictive control of a multiscale thin film deposition process using artificial neural networks, Chem. Eng. Sci. 207 (2019) 1230–1245, https://doi.org/10.1016/j.ces.2019.07.044.

[43] L. Banko, Y. Lysogorskiy, D. Grochla, D. Naujoks, R. Drautz, A. Ludwig, Predicting structure zone diagrams for thin film synthesis by generative machine learning, Commun. Mater. 1 (2020) 15, https://doi.org/10.1038/s43246-020-0017-2.

[44] J. Peng, R. Pillai, M. Romedenne, B.A. Pint, G. Muralidharan, J. Allen Haynes, D. Shin, Data analytics approach to predict high-temperature cyclic oxidation kinetics of NiCr-based alloys, Npj Mater. Degrad. 5 (2021) 41, https://doi.org/10.1038/s41529-021-00188-z.

[45] B. Jia, Q. Wan, L. Yan, Y. Luo, Q. Wei, C. Niu, B. Yang, S. Li, L. Meng, Tribological properties and machine learning prediction of FeCoCrNiAlN high entropy coatings, Surf. Coat. Technol. 477 (2024) 130341, https://doi.org/10.1016/j.surfcoat.2023.130341.

[46] X. Xu, X. Wang, S. Wu, L. Yan, T. Guo, K. Gao, X. Pang, A.A. Volinsky, Design of super-hard high-entropy ceramics coatings via machine learning, Ceram. Int. 48 (2022) 32064–32072, https://doi.org/10.1016/j.ceramint.2022.07.145.

[47] G. Wang, J. Song, G. Zhao, Q. Ding, T. Yin, H. Wang, Tribological performance prediction of WS_2 coating under different conditions by machine learning, Wear 532-533 (2023) 205092, https://doi.org/10.1016/j.wear.2023.205092.

[48] H. Ma, P. Qin, Y. Cui, R. Liu, P. Ke, F. Wang, L. Liu, Prediction of multilayer Cr/GLC coatings degradation in deep-sea environments based on integrated mechanistic and machine learning models, Corros. Sci. 224 (2023) 111513, https://doi.org/10.1016/j.corsci.2023.111513.

[49] K. Yuan, R. Eriksson, R. Lin Peng, X.-H. Li, S. Johansson, Y.-D. Wang, Modeling of microstructural evolution and lifetime prediction of MCrAlY coatings on nickel based superalloys during high temperature oxidation, Surf. Coat. Technol. 232 (2013) 204–215, https://doi.org/10.1016/j.surfcoat.2013.05.008.

[50] K. Yuan, R. Eriksson, R. Lin Peng, X.-H. Li, S. Johansson, Y.-D. Wang, MCrAlY coating design based on oxidation-diffusion modelling. Part I: microstructural evolution, Surf. Coat. Technol. 254 (2014) 79–96, https://doi.org/10.1016/j.surfcoat.2014.05.067.

[51] M. Elsaß, M. Frommherz, A. Scholz, M. Oechsner, Interdiffusion in MCrAlY coated nickel-base superalloys, Surf. Coat. Technol. 307 (2016) 565–573, https://doi.org/10.1016/j.surfcoat.2016.09.049.
[52] K. Yuan, R. Lin Peng, X.-H. Li, S. Johansson, Hot corrosion behavior of HVOF-sprayed CoNiCrAlYSi coatings in a sulphate environment, Vacuum 122 (2015) 47–53, https://doi.org/10.1016/j.vacuum.2015.09.015.
[53] Y. Pan, L. Zhang, Z. Huang, L. Jiang, Coarsening behavior of γ′ precipitates of single crystal Ni-based superalloys during long-term exposure, Mater. Lett. 241 (2019) 210–213, https://doi.org/10.1016/j.matlet.2019.01.066.
[54] C.K.L. Davies, P. Nash, R.N. Stevens, The effect of volume fraction of precipitate on ostwald ripening, Acta Metall. 28 (1980) 179–189, https://doi.org/10.1016/0001-6160(80)90067-X.
[55] C. Li, K. Xu, M. Lou, L. Wang, K. Chang, Machine learning-enabled prediction of high-temperature oxidation resistance for Ni-based alloys, Corros. Sci. 234 (2024) 112152, https://doi.org/10.1016/j.corsci.2024.112152.